ACS APPLIED MATERIALS & INTERFACES

Research Article

www.acsami.org

Investigating the Mg−Si Binary System via Combinatorial Sputter Deposition As High Energy Density Anodes for Lithium-Ion Batteries

Guido Schmuelling,* Martin Winter, and Tobias Placke*

University of Muenster, MEET Battery Research Center, Institute of Physical Chemistry, Corrensstrasse 46, 48149 Muenster, Germany

ABSTRACT: Mg−Si thin films with various elemental compositions ranging from $0 \leq x \leq 1$ in $Mg_xSi_{(1-x)}$ were obtained via combinatorial magnetron sputter deposition of Si and Mg in order to improve the electrochemical lithiation/delithiation process of pure Si by embedding Si in an active Mg−Si matrix. Scanning electron microscopy, energy-dispersive X-ray spectroscopy, X-ray diffraction, and Raman spectroscopy methods were used to investigate the morphology, stoichiometry, and structure of the different thin film samples. Constant current charge/discharge cycling revealed significant electrochemical changes depending on the Mg content in comparison to the pure Si active material improving the capacity retention to 96% over 400 cycles.

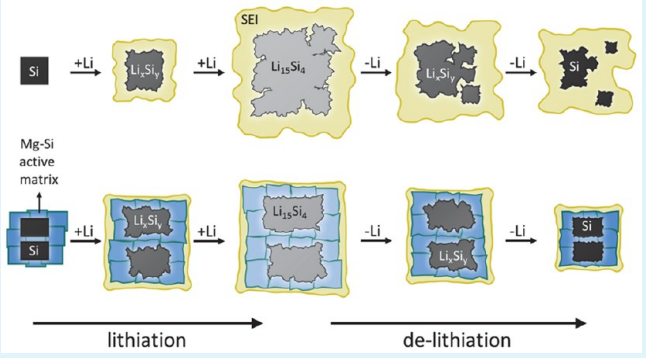

KEYWORDS: *silicon, magnesium, combinatorial magnetron sputter deposition, lithium-ion battery, active matrix*

1. INTRODUCTION

Lithium-ion technology has had an enormous impact on both the research as well as the industrial community during the past decades.[1−4] In addition to their use in portable electronics, lithium-ion batteries are used in plug-in hybrid (PHEVs) and battery electric vehicles (BEVs) and have been increasingly used in hybrid electric vehicles (HEVs) as well. In order to achieve a better market penetration of BEVs it is necessary to substantially increase the range of such vehicles while simultaneously reducing their cost.[5] It is therefore important to enhance the gravimetric (Wh kg^{-1}) and volumetric energy (Wh L^{-1}) density of the lithium-ion battery, which can be accomplished by either using cathode active materials with an enhanced operating potential and/or by developing electrode materials with higher specific capacity.[6] Even with state-of-the-art cathodes, switching from the usually deployed graphite (specific capacity = 372 mAh g^{-1}, not regarding the weight of the intercalated Li[7]) to anodes that offer a capacity on the order of 1000 mAh g^{-1} can significantly increase the total specific capacity at the cell level.[8] Therefore, the design of novel high energy density anode materials seems imperative.

One of the most popular reactions to replace the intercalation process of Li into graphitic carbon is the alloying reaction of Li inserting into Si, yielding a theoretical specific capacity of 3579 mAh g^{-1} (excluding the weight of the stored Li) at room temperature.[9] However, pure Si suffers greatly from enormous volume expansion/contraction upon lithiation/delithiation, which causes loss of active material and continuous electrolyte degradation, ultimately leading to poor capacity retention and short cycle life.[10] One strategy to overcome these issues with Li storage metals such as Sn and Si is to embed the metal in a buffering matrix,[8,11] which itself can be active (e.g., graphite,[12] $CrSi_2$[13] or Si−Ag[14]) or inactive (e.g., Ni−Si,[15,16] Fe−Si[17] or Ti−Si[18,19]) toward lithiation. Focusing on Mg as a secondary element, it has been demonstrated and understood that the intermetallic phase in the Mg−Si binary system, Mg_2Si (Figure 1),[20] is able to reversibly insert and deinsert Li with a reasonable delithiation capacity (1074 mAh g^{-1}) but an insufficient capacity retention.[21−26] On the very left-hand side of the phase diagram (Figure 1), Mg itself, although it is very attractive as an active buffering matrix because of a very broad solid-solution Li−Mg region, suffers from only partially reversible Li extraction and high reactivity.[27,28]

In this contribution, we investigate the Mg−Si binary system throughout the whole phase diagram, which has not been reported in literature so far. By utilizing the physical method of combinatorial magnetron sputter deposition, we are able to obtain thin films in any desired composition in order to understand and optimize their electrochemical performance with regard to long-term cycling stability while retaining a specific capacity of at least 1000 mAh g^{-1}. Therefore, we conduct constant current charge/discharge cycling experiments and characterize the thin films with respect to their stoichiometry and morphology by using scanning electron microscopy (SEM), energy-dispersive X-ray spectroscopy (EDX), Raman spectroscopy, and X-ray diffraction (XRD). The Mg−Si thin film model system presented in this paper contributes to a deeper understanding and facilitates the application of Mg−Si alloy anodes in the future.

Received: June 17, 2015
Accepted: August 27, 2015
Published: August 27, 2015

DOI: 10.1021/acsami.5b05382
ACS Appl. Mater. Interfaces 2015, 7, 20124−20133

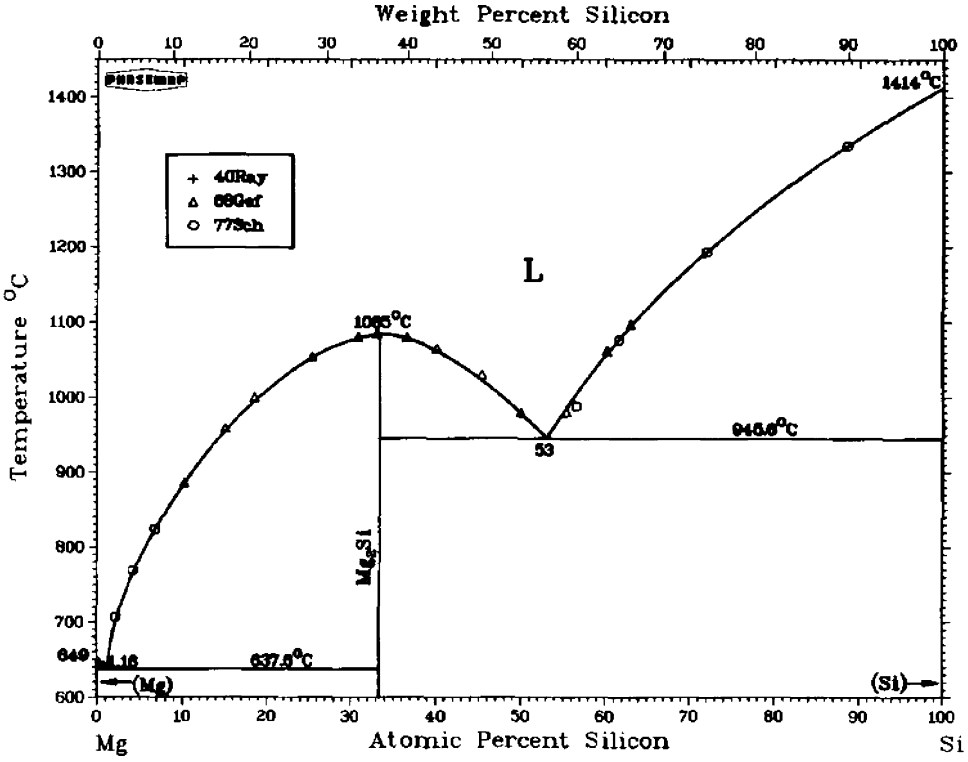

Figure 1. Binary alloy phase diagram for the Mg−Si system (reprinted with permission of Springer Science+Business Media).[20]

2. EXPERIMENTAL SECTION

Mg−Si thin films were produced via combinatorial RF magnetron sputter deposition (further referred to as cosputtering) in a custom designed Bestec sputter device with a base pressure of approximately 5.0 × 10^{-8} mbar. Films with various elemental compositions ranging from 0 ≤ x ≤ 1 in $Mg_xSi_{(1-x)}$ were obtained by altering the applied RF-power on both the Si (≥99.9%, Ø = 4 in., FST GmbH) and the Mg (≥99.98%, Ø = 2 in., HMW Hauner) target according to Table 1. The thin films were simultaneously cosputtered onto a dendritic copper foil substrate (thickness = 20 μm, Ø = 3 in., Schlenk) for electrochemical investigations and onto a Si-wafer (Siltronic) in order to track the film thickness, which was investigated after deposition with a DektakXT Profilometer (Bruker). While the Si target was located directly opposite to the rotating substrate holder, the Mg target was tilted toward the substrate at an angle of 35°. To obtain a comparable amount of Si in the different samples, we set the deposition time for each sample to 1 h with an Ar plasma working pressure of 5.0 × 10^{-3} mbar. After deposition, electrodes with a diameter of 12 mm were cut out of the copper substrate and stored in an argon filled glovebox (UniLab, MBraun) with water and oxygen vapor contents below 1 ppm. The electrode active weight had to be calculated based on an average mass loading obtained from the 3 in. substrate as the active mass of a single electrode is way too low.

Table 1. Summary of Mg−Si Thin Film Deposition Experiments via RF Magnetron Cosputtering

growth ID	applied RF-power Mg (W)	applied RF-power Si (W)	film thickness (nm) (±3)	electrode active weight (mg cm^{-2}) (±0.002)	x in $Mg_xSi_{(1-x)}$ via EDX (±0.01)
Si	0	95	250	0.057	0.00
SiMg26	20	95	300	0.061	0.26
SiMg40	30	95	320	0.073	0.40
SiMg51	40	95	395	0.078	0.51
SiMg61	50	95	425	0.089	0.61
SiMg65	60	95	465	0.103	0.65
SiMg82	60	50	337	0.063	0.82
Mg	50	0	185	0.040	1.00

Energy-dispersive X-ray spectroscopy (EDX) was used to investigate the elemental composition of the various Mg−Si thin films in an Auriga CrossBeam workstation from Zeiss. Therefore, rectangular spot measurements with an approximate area of 50 μm^2 were conducted several times at different spots of the deposited thin film to obtain reliable average elemental compositions with corresponding standard deviations below 1%. The electron beam was maintained at 15 kV, while the EDX signal was detected with an X-Max 80 mm^2 detector and evaluated with the INCA software, both from Oxford Instruments. SEM was used to investigate the thin film electrode morphology before and after electrochemical cycling experiments. The samples were analyzed with the Auriga CrossBeam workstation from Zeiss at an acceleration voltage of 3 kV.

Raman spectroscopy investigations were carried out using a Bruker Senterra dispersive Raman microscope equipped with a green 532 nm laser and a 20× objective. The laser power was adjusted to 5 mW while recording the Raman spectra with 20 integrations and an integration time of 10 s.

X-ray diffraction measurements were conducted using a Bruker D8 Advance X-ray diffractometer equipped with a copper target X-ray tube in a range between 2θ = 10 and 90° with a step size of 0.01° per 1.5 s resulting in 200 min per XRD scan at an accelerating voltage of 40 kV and a current flow of 30 mA.

Electrochemical investigations were carried out in lab-scale, Swagelok type T-cells with a three-electrode configuration assembled in an Ar-filled glovebox. In all half-cell measurements, high-purity metallic lithium foil (Rockwood Lithium) was used as counter (Ø = 12 mm) and reference (Ø = 6 mm) electrode. A glass microfiber filter (Whatman, grade GF/D) as a separator and battery grade EC/DEC 3:7 (w/w) with 2 wt % VC and 1 M $LiPF_6$ (all from UBE) as electrolyte solution was used.

Charge/discharge cycling was performed on a multichannel Maccor 4300 battery test system. The current (I) for the constant current steps of both the charge and discharge of 400 consequent cycles was set in a manner corresponding to 1 μA per nm in film thickness in order to establish a comparable strain on the Mg−Si thin films. First, three

DOI: 10.1021/acsami.5b05382
ACS Appl. Mater. Interfaces 2015, 7, 20124−20133

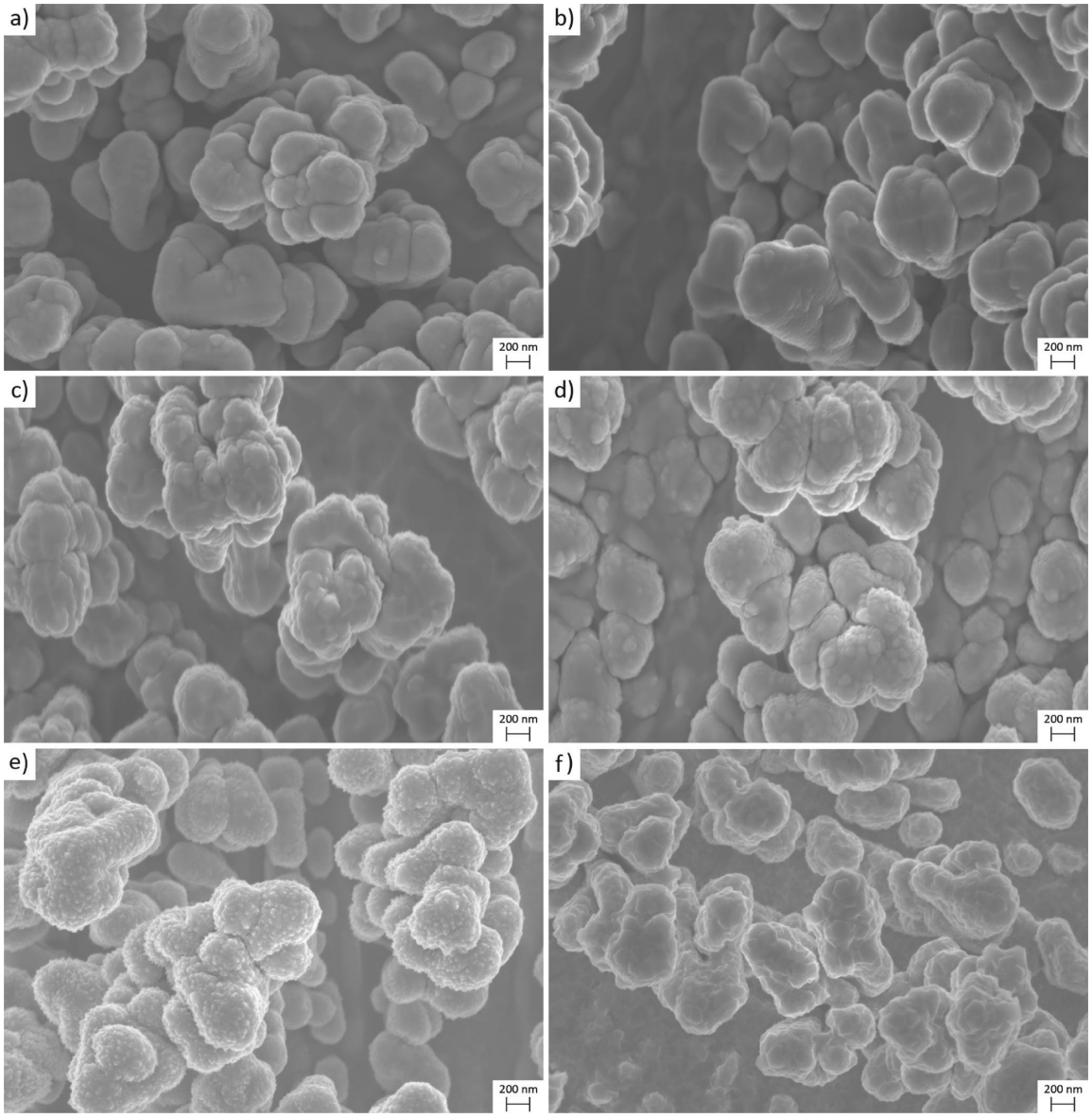

Figure 2. SEM pictures of the as-prepared (a) Si, (b) SiMg26, (c) SiMg51, (d) SiMg65, (e) SiMg82, and (f) Mg thin film.

formation cycles with 0.1 × *I* were performed. The operating potential range was set between 1.5 and 0.040 V vs Li/Li^+. In addition, a constant potential step (CPS) at the lower cutoff potential was applied in each cycle after the constant current sequence until the remaining current flow was less than 0.05 × *I*. Electrochemical impedance spectroscopy (EIS) measurements were conducted on a VSP multichannel potentiostat/galvanostat with frequencies from 100 mHz to 1 MHz and an amplitude of 10 mV on galvanostatically cycled thin film samples at 50% state of charge (SOC) after a 30 min rest step. All experiments were carried out in climatic chambers at a temperature of 20 °C.

3. RESULTS AND DISCUSSION

3.1. Morphological and stoichiometric characterization of the Mg−Si thin films. Magnetron sputter deposition of a multicrystalline Si target at a power of 95 W for 1 h resulted in a 250 nm thin film (Table 1), which we chose to serve as our reference system. Consequently, in order to obtain homogeneously distributed Mg−Si thin film samples with various compositions, cosputtering was facilitated by gradually increasing the applied power on a Mg target from 0 to 60 W yielding in thin films with Mg contents as high as 65% according to EDX investigations. Decreasing the power applied on the Si target resulted in a Mg−Si thin film, which offered a composition above the Mg_2Si stoichiometry (SiMg82). For completion, a pure 185 nm thin Mg film was obtained by solely sputtering Mg at 50 W.

Figure 2 displays SEM pictures of different thin films deposited on dendritic copper foil, which induces the coagulative structure for all thin films during the deposition process. We chose dendritic instead of smooth copper foil as substrate and current collector due to its superior adhesive and mechanical properties and because it offers the active material more vacant space, which is beneficial during the lithiation process and the corresponding volume expansion. The pure Si thin film (Figure 2a) appears amorphous with no obvious crystal structure. With increasing Mg content the Mg−Si thin films lose their smooth amorphous structure and start to gain crystal orientations. The pure Mg sample morphology reveals its very distinct hexagonal close-packed structure (Figure 2f) leading to the conclusion that we might be able to observe a corresponding X-ray diffraction pattern, even for the rather thin samples (<500 nm).

DOI: 10.1021/acsami.5b05382
ACS Appl. Mater. Interfaces 2015, 7, 20124−20133

Figure 3 displays the diffraction patterns of the Mg−Si thin films with various elemental compositions. Up to and including

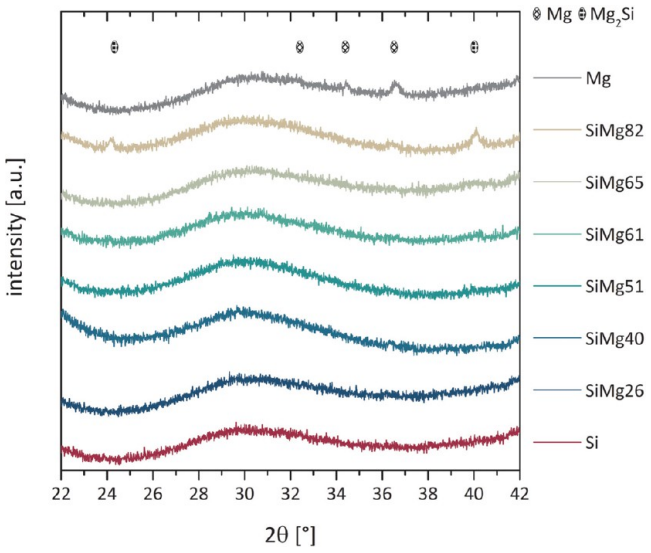

Figure 3. X-ray diffraction pattern of the as-prepared Mg−Si thin films with various elemental compositions.

the SiMg65 composition, the thin films do not exhibit any diffraction peaks suggesting a predominantly amorphous structure. However, the SiMg82 and the Mg sample show the two major diffraction peaks for the CaF_2-like Mg_2Si (24.2 and 40.1°, ICDD PDF 04-014-4260) and the $P6_3/mmc$ Mg structure (34.4 and 36.6°, ICDD PDF 04-004-8745), respectively.

To further investigate the Mg−Si stoichiometry, we conducted Raman scattering experiments (Figure 4). The Si thin film exhibits its expected spectrum with the typical phonon bands of amorphous Si: the transverse optical (TO) at 469 cm^{-1}, the longitudinal optical (LO) at roughly 378 cm^{-1}, the longitudinal

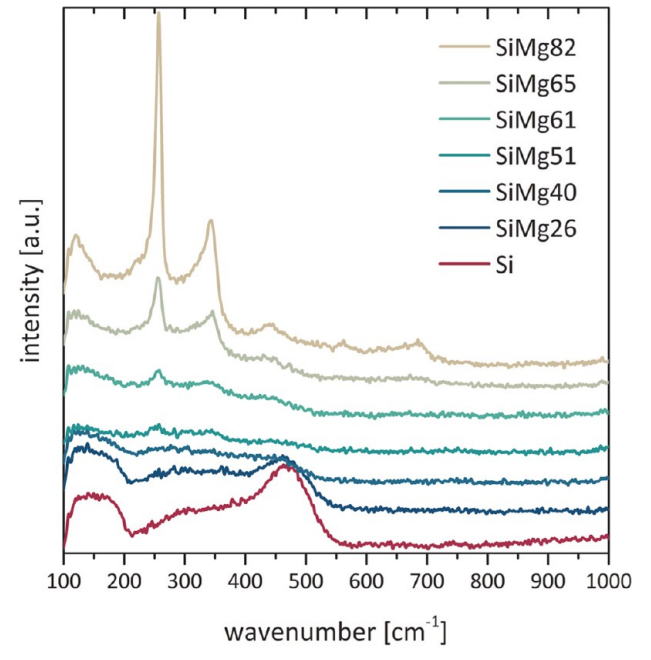

Figure 4. Raman spectra of the as prepared Mg−Si thin films with various elemental compositions.

acoustic (LA) at about 300 cm^{-1}, and the transverse acoustic (TA) at 150 cm^{-1}.[29] When the Mg content increases, the peaks of amorphous Si gradually decrease until they vanish for the SiMg51 sample. Further increasing the Mg/Si ratio induces a new peak to appear at 256 cm^{-1} (SiMg61). When considering the higher Mg content samples, we identified this peak and another one at 345 cm^{-1} as the F_{2g} and the F_{1u} phonon band of Mg_2Si, respectively.[30−35] The highest Mg content sample (SiMg82) also shows the 2LO overtone around 690 cm^{-1} and three further bands, two of which have been demonstrated and interpreted as overtones by Onari et al.[35] (440 cm^{-1} and 580 cm^{-1}) and one peak at 120 cm^{-1} that has not been identified so far but might be representing a Mg phase that is already present in the SiMg82 sample, which is slightly indicated in the XRD as well. Note that the pure Mg sample could not be displayed due to high fluorescence.

3.2. Electrochemical Investigations of the Mg−Si Thin Films. Figure 5 displays the results of the constant current/

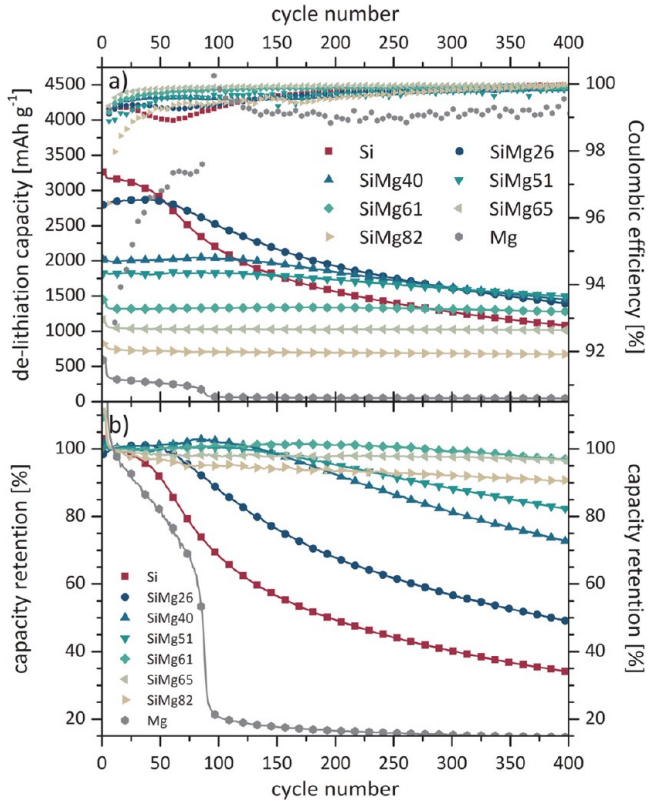

Figure 5. (a) Delithiation capacities and Coulombic efficiencies and (b) the corresponding capacity retentions based on the 10th cycle vs cycle number for the constant current/constant potential charge/discharge cycling of Mg−Si thin films with various elemental compositions.

constant potential charge/discharge cycling of the investigated Mg−Si thin films with various elemental compositions. Besides the delithiation capacity and Coulombic efficiency (Figure 5a), the capacity retention based on the 10th cycle is also depicted (Figure 5b). The latter parameter enables a legitimate comparison due to the fact that the specific delithiation capacities are based on a calculated mass loading. Table 2 summarizes the electrochemical key figures for the galvanostatic charge/discharge experiment. Among these, we also calculated the applied delithiation current rate in the 10th cycle for comparison reasons. Due to the lack of information about the specific

DOI: 10.1021/acsami.5b05382
ACS Appl. Mater. Interfaces 2015, 7, 20124−20133

Table 2. Electrochemical Key Figures of the Investigated Mg−Si Thin Films

growth ID	initial delithiation capacity (mAh g^{-1}) (±1.9%)	initial Coulombic efficiency (%) (±1.5)	calculated delithiation rate of 10th cycle	200th cycle delithiation capacity (mAh g^{-1}) (±1.9%)	200th cycle Coulombic efficiency (%) (±0.04)	400th cycle capacity retention (%) (±0.2)
Si	3262	70.8	1.1C	1564	99.8	34.1
SiMg26	2794	76.7	1.5C	1927	99.7	49.0
SiMg40	2012	69.3	1.9C	1842	99.6	72.6
SiMg51	1822	64.9	2.5C	1731	99.6	82.1
SiMg61	1447	63.7	3.2C	1336	99.9	96.9
SiMg65	1163	72.4	3.8C	1028	> 99.9	96.8
SiMg82	827	54.6	6.4C	695	99.6	90.6
Mg	594	29.3	13.6C	54	99.0	14.6

delithiation capacities of the investigated Mg−Si thin films, we chose a current rate I that corresponds to 1 μA per nm in film thickness. The resulting C-rates naturally increase with increasing Mg content as the specific delithiation capacity of the samples gradually decreases. However, the effect of different C-rates is known to be rather small for thin films,[36] especially when a constant potential step eventually ensures a fully lithiated anode, which is confirmed in this experiment as the electrochemical results do not suffer from an increasing C-rate. To an extent, the contrary is the case. Starting with the pure Si thin film sample we are able to obtain an initial capacity above 3000 mAh g^{-1} with a Coulombic efficiency of 71%. However, the reversible capacity quickly fades in a very typical behavior for Si thin films.[37,38] As expected, increasing the Mg content gradually decreases the initial specific delithiation capacity, for example, to 1028 mAh g^{-1} for the SiMg65 thin film (Table 2). However, the capacity fading also decreases significantly. Adding Mg amounts as low as 26% already delivers a stable delithiation capacity up to cycle 50 and increases the capacity retention in the 400th cycle from 34.1 to 49.0%. Thin films with a Mg content up to 51% exhibit a stable cycling with a reversible capacity above 1800 mAh g^{-1} for roughly 150 cycles with a slightly decreased Coulombic efficiency but a capacity retention exceeding 80% in the 400th cycle. After a short initial capacity loss, which appears like a formation process, the samples SiMg61 to SiMg82 show basically no capacity fading anymore, and the Coulombic efficiencies and capacity retentions reach values above 99.6% and 90%, respectively. The delithiation capacities in the 200th cycle are 1731 and 1028 mAh g^{-1}, respectively. Of all the Mg−Si thin films, the SiMg65 sample stands out with a Coulombic efficiency above 99.9% in the 200th cycle and a capacity retention of 96.8% after 400 cycles with a corresponding delithiation capacity just slightly above the target of 1000 mAh g^{-1}. Especially considering that the SiMg65 film has been effectively cycled at roughly 3.8 C, compared to 1.1 C at the pure Si sample due to the chosen (film thickness-based) current rate, the long-term cycling behavior has been improved significantly. For completion of the data set, the pure Mg thin film shows a rapid capacity decay and a poor cycling efficiency.

One important parameter to consider when interpreting the electrochemical performance is the Coulombic efficiency, which indicates the discrepancy between charge and discharge due to parasitic side reactions, which can be connected to Li loss or electrolyte decomposition due to solid electrolyte interphase (SEI) formation.[39] This inefficiency (CIE) is intuitively accessible when plotted accumulatively vs the cycle number (Figure 6).[40−42] The pure Si and lower Mg content thin films exhibit a comparable inefficiency during the first 50 cycles, whereupon the inefficiency decreases with increasing Mg-amount. Although it starts in the same fashion, the SiMg61

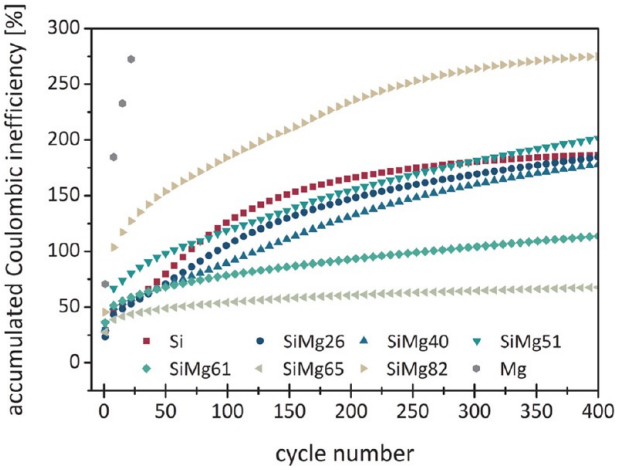

Figure 6. Accumulated CIE vs cycle number for the constant current/constant potential charge/discharge cycling of Mg−Si thin film electrodes with various elemental compositions.

sample displays a significantly slower progressing inefficiency. The best efficiency is clearly obtained with a Mg content of 65%. Despite the rather stable cycling results (Figure 5a), the SiMg82 thin film shows a rather high inefficiency, indicating a high Li loss, electrolyte decomposition, or both, which is probably not observed during the constant current cycling experiment due to the Li counter electrode offering the system a large Li excess. This inefficiency can only be exceeded by the poor performance of pure Mg.

Figure 7 displays the differential capacity profiles of the first cycle of the constant current charge/discharge cycling experiment. The close-up of the typical potential region where the SEI formation occurs (Figure 7b) clearly exhibits significant differences. The charge consumed above the peak at roughly 1.2 V vs Li/Li^+,[43] which can be attributed to the reduction of the electrolyte additive VC, the peak itself and the reduction processes around 1.0 to 0.6 V vs Li/Li^+ (mostly degradation of the cyclic and linear carbonate solvent molecules[43]) all decrease with increasing Mg content up to the composition of SiMg65. Further increasing the Mg-amount also increases the irreversible electrolyte reduction, which can be attributed to the high reactivity of Mg.[27,28]

The first lithiation process is highlighted in Figure 7c. The pure Si thin film shows the typical broad insertion peaks of amorphous Si at 0.3 and 0.1 V vs Li/Li^+.[44] Up to the SiMg65 thin film sample, the onset potential for the first lithiation peak gradually shifts to lower potentials with increasing Mg contents (0.26 V vs Li/Li^+ in the case of SiMg65), while the secondary insertion peak vanishes. In addition, the thin films with an intermediate Mg-amount of

DOI: 10.1021/acsami.5b05382
ACS Appl. Mater. Interfaces 2015, 7, 20124−20133

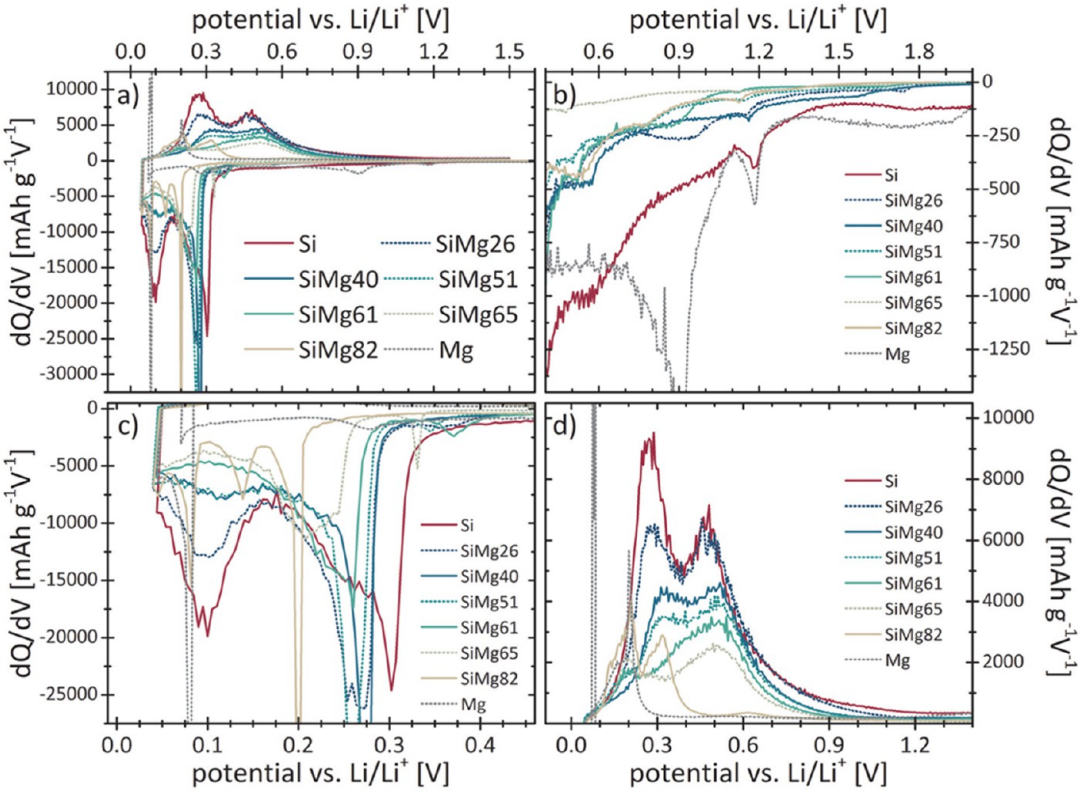

Figure 7. (a) Differential capacity vs potential plots displaying the first constant current charge/discharge cycle of Mg−Si thin films with various elemental compositions. Typical potential regions for (b) electrolyte decomposition, (c) lithiation and (d) delithiation are enlarged.

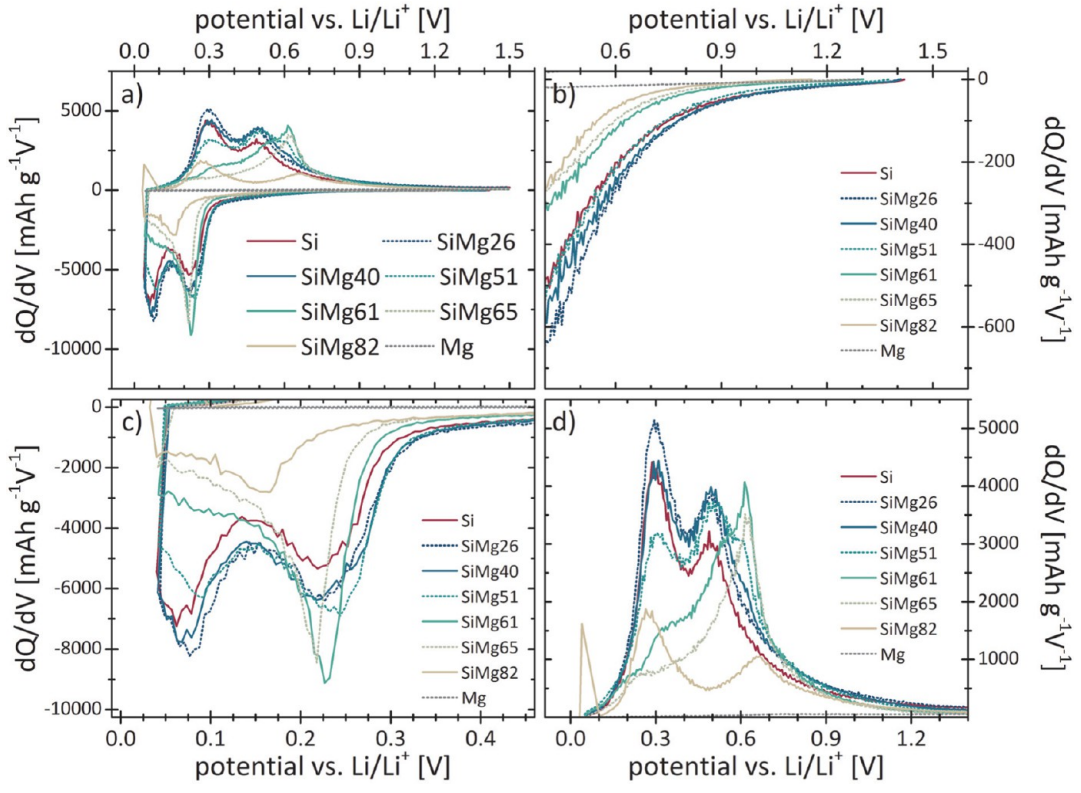

Figure 8. Differential capacity vs potential plots displaying the 200th constant current charge/discharge cycle (a) of Mg−Si thin films with various elemental compositions. Typical potential regions for (b) electrolyte decomposition, (c) lithiation, and (d) delithiation are enlarged.

SiMg50 to SiMg65 display a small cathodic peak around 0.35 V vs Li/Li^+, which disappears directly in the second cycle, suggesting an irreversible process. The SiMg82 thin film displays a typical lithiation profile of Mg_2Si with the two corresponding insertion

DOI: 10.1021/acsami.5b05382
ACS Appl. Mater. Interfaces 2015, 7, 20124−20133

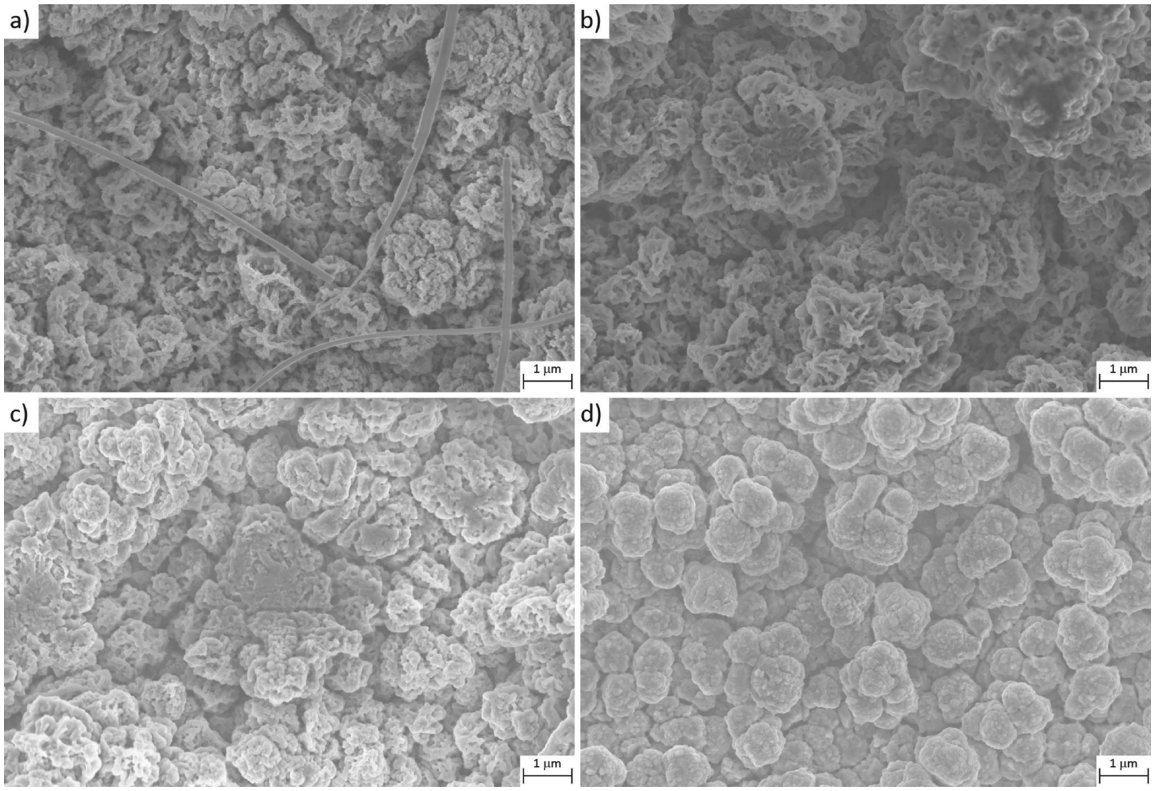

Figure 9. SEM pictures of (a) Si, (b) SiMg26, (c) SiMg51, and (d) SiMg65 thin films after 400 constant current charge/discharge cycles.

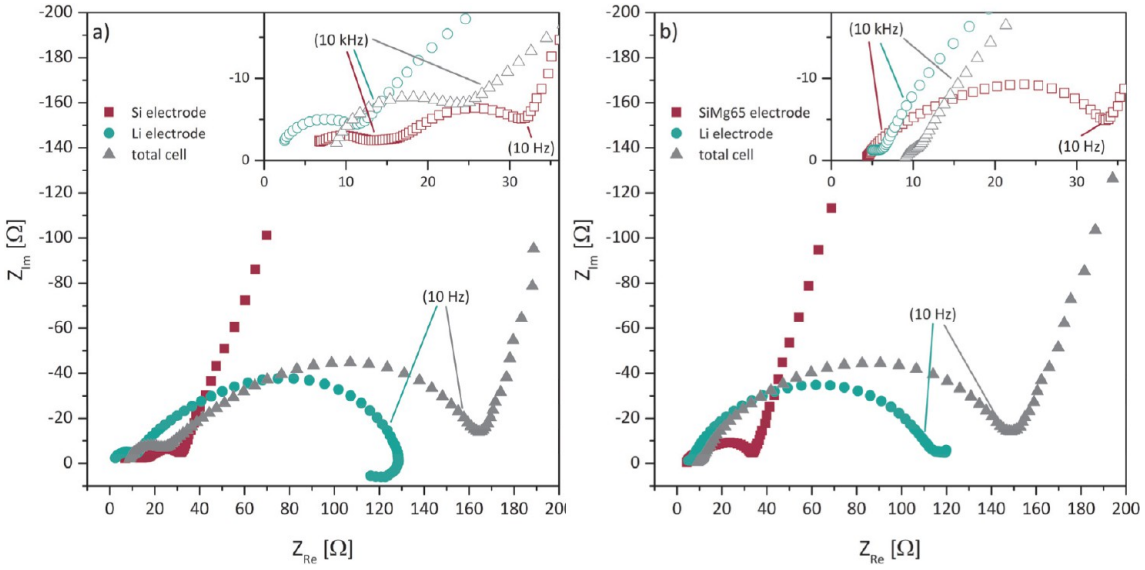

Figure 10. Impedance spectra of (a) Si and (b) SiMg65 thin film half cells at 50% state of charge in the 100th delithiation step. (Insets) Detailed views of the impedance response in the high-frequency regions.

peaks at 0.2 and 0.14 V vs Li/Li^+, as well as a third one that overlaps with the insertion peak of the pure Mg sample at 0.08 V vs Li/Li^+ following the accepted lithiation mechanism for Mg_2Si, in which a Mg phase is electrochemically obtained.[24−26,45] In our case, a minor Mg phase is already present in the sample, which intensifies this effect. During deinsertion (Figure 7d), these two samples also share their first anodic peak at 0.21 V vs Li/Li^+, while the SiMg82 sample shows two more peaks at 0.3 and 0.6 V vs Li/Li^+ corresponding to the delithiation of Mg_2Si (note that the sharp spike in the Mg sample originates from a short increase in potential during galvanostatic lithiation and does not belong to the deinsertion process). In the case of the pure Si thin film, we obtain the expected delithiation peaks corresponding to amorphous Si at potentials of 0.27 and 0.48 V vs Li/Li^+.[37,38] While the former peak gradually vanishes with increasing Mg content, the latter one stays though getting smaller due to the decrease in specific capacity.

The differential capacity profile of the 200th constant current charge/discharge cycle (Figure 8a) emphasizes the differences of the investigated thin films upon long-term cycling. Samples

DOI: 10.1021/acsami.5b05382
ACS Appl. Mater. Interfaces 2015, 7, 20124−20133

containing up to 51% Mg show a higher charge consumption between 1.2 and 0.5 V vs Li/Li^+, indicating a higher fraction of continuous electrolyte degradation on freshly formed Li/Si−Mg surfaces due to large volume expansion/contraction, than the higher Mg content samples (Figure 8b). Furthermore, they display a very similar lithiation profile (Figure 8c) with two broad cathodic peaks at 0.25 and 0.06 V vs Li/Li^+, which are slightly shifted to lower potentials compared to the first cycle, most likely originating from an increased SEI resistance. In the SiMg61 and SiMg65 thin films, the latter peak dissipates, while the former one sharpens and gradually shifts to 0.21 V vs Li/Li^+. In the SiMg82 sample, there is only one very broad lithiation peak remaining at 0.15 V vs Li/Li^+, indicating a more solid-solution type reaction than in the first cycle presumable due to a higher degree of amorphization within the active material. However, upon delithiation (Figure 8d), the anodic peaks of Mg_2Si are retained. Up to a Mg content of 51%, the deinsertion profiles appear typical compared to amorphous Si, although with increasing Mg-amount the ratio of the two delithiation peaks at 0.3 and 0.5 V vs Li/Li^+ decreases. The SiMg61 and SiMg65 thin films exhibit a sharper anodic peak that shifts to 0.6 V vs Li/Li^+ with a minor shoulder at 0.3 V vs Li/Li^+.

After the constant current charge/discharge cycling experiment, the investigated thin film electrodes were characterized with respect to their morphology by means of scanning electron microscopy (Figure 9). The pictures emphasize the conclusions made for the results obtained during cycling. The pure Si thin film (Figure 9a) shows an enormous SEI formation and most likely loss of active material, equivalent to loss of contact. During cycling the film even grew into the separator, whose glass fibers are encapsulated in the active material. Increasing the Mg content gradually decreases this behavior. The volume expansion and SEI formation is inhibited significantly. The SiMg65 thin film sample almost retains its original morphology, therefore explaining the superior cycling performance.

To validate the beneficial effect of the active matrix concept, namely the depression of electrolyte decomposition and SEI growth, we conducted EIS measurements. Figure 10 displays the impedance response of the Si and the SiMg65 thin film sample during the 100th delithiation cycle at 50% SOC. The investigations were carried out according to Ender et al., which enables monitoring the working electrode (Si and SiMg65) as well as the lithium counter electrode and the total cell impedance.[46] However, due to geometrical and electrical asymmetry, the impedance response is likely to be distorted. Furthermore, the nature of the investigated thin films, namely various thin film thicknesses, different Li-ion concentrations at 50% state of charge and corresponding open circuit potentials as well as different Li-ion diffusion coefficients, prohibit a direct comparison of absolute impedance values. Nevertheless, the widely accepted phenomena for negative electrodes,[47−51] depressed semicircles generated at high-to-mid frequencies, and linear trends at low frequencies can be observed very clearly. The pure Si thin film (Figure 10a) displays two separate, depressed semicircles: one below 10 kHz and one between 1 kHz and 10 Hz. The former is generally connected to Li ion migration through surface layers, while the latter expresses the Li ion transfer through interfaces. The same is true for the Li counter electrode. However, the transfer resistance is much more pronounced, while the surface layer term below 10 kHz has a similar value. The inductive loop at very low frequencies has been observed and attributed to electrical asymmetry in the past.[46] In contrast to the linear incline in the Si electrode, there is obviously no solid-state diffusion of Li-ions at the counter electrode observable. The total cell impedance response is the sum of both electrodes, which can be well identified by the ohmic resistance at the highest frequency and the sum of the surface transfer and diffusion terms. Figure 10b displays the impedance response of the SiMg65 thin film cell. In contrast to the pure Si sample, the surface term below 10 kHz for the SiMg65 electrode is not distinguishable and therefore much less pronounced, indicating a smaller impedance contribution of the surface layer. Furthermore, the surface term for the Li counter electrode is smaller as well, which is probably connected to the significantly higher Coulombic efficiency of the SiMg65 sample and the correspondingly inhibited irreversible loss of Li (as displayed in Figure 6).

4. CONCLUSION

In summary, we presented the electrochemical lithiation and delithiation behavior of various stoichiometric samples across the Si−Mg binary phase diagram. We facilitated RF magnetron cosputter deposition to obtain thin film samples with a variety of different compositions and investigated their morphology, structure and constitution via SEM, EDX, XRD, and Raman spectroscopy. By adding Mg to the Si active material the long-term cycling behavior can be gradually improved. A Mg content just below the Mg_2Si stoichiometry exhibits the desired 1000 mAh g^{-1} of anode capacity (considering state-of-the-art cathodes), a capacity retention as high as 96% after 400 consequent constant current charge/discharge cycles at roughly 3.8C with a Coulombic efficiency above 99.9%. Therefore, it is a very promising candidate as an anode active material for next generation lithium-ion batteries. This overall best performance originates from decreased volume expansion/contraction upon insertion/deinsertion of Li, consequently less electrolyte decomposition/degradation during SEI formation, a thinner SEI surface layer and inhibited loss of active material. Mg contents above the Mg_2Si stoichiometry exhibit an enhanced inefficiency due to the high reactivity of Mg and are therefore not suitable for application.

AUTHOR INFORMATION

Corresponding Authors

*E-mail: g.schmuelling@uni-muenster.de. Phone: +49 251 83-36785. Fax: +49 251 83-36032.

*E-mail: tobiasplacke@uni-muenster.de. Phone: +49 251 83-36701. Fax: +49 251 83-36032.

Author Contributions

All authors have given approval to the final version of the manuscript.

Notes

The authors declare no competing financial interest.

ACKNOWLEDGMENTS

The authors gratefully acknowledge the supply of materials by Rockwood Lithium (metallic lithium foil), FST Freiberg (silicon target) and Hauner Metallische Werke (magnesium target) as well as the funding of the project “Pouch-Zelle” (funding code 64.65.69, EM 1024 C) by the state NRW within the NRW Ziel 2-Programm (EFRE), Germany.

REFERENCES

(1) Winter, M.; Brodd, R. J. What Are Batteries, Fuel Cells, and Supercapacitors? *Chem. Rev.* **2004**, *104* (10), 4245−4269.

DOI: 10.1021/acsami.5b05382
ACS Appl. Mater. Interfaces 2015, 7, 20124−20133

(2) Armand, M.; Tarascon, J. M. Building Better Batteries. *Nature* **2008**, *451* (7179), 652−657.
(3) Goodenough, J. B.; Kim, Y. Challenges for Rechargeable Li Batteries. *Chem. Mater.* **2010**, *22* (3), 587−603.
(4) Wagner, R.; Preschitschek, N.; Passerini, S.; Leker, J.; Winter, M. Current Research Trends and Prospects among the Various Materials and Designs Used in Lithium-Based Batteries. *J. Appl. Electrochem.* **2013**, *43* (5), 481−496.
(5) Andre, D.; Kim, S.-J.; Lamp, P.; Lux, S. F.; Maglia, F.; Paschos, O.; Stiaszny, B. Future Generations of Cathode Materials: An Automotive Industry Perspective. *J. Mater. Chem. A* **2015**, *3* (13), 6709−6732.
(6) Goriparti, S.; Miele, E.; De Angelis, F.; Di Fabrizio, E.; Zaccaria, R. P.; Capiglia, C. Review on Recent Progress of Nanostructured Anode Materials for Li-Ion Batteries. *J. Power Sources* **2014**, *257*, 421−443.
(7) Kohs, W.; Santner, H. J.; Hofer, F.; Schrottner, H.; Doninger, J.; Barsukov, I.; Buqa, H.; Albering, J. H.; Möller, K. C.; Besenhard, J. O.; Winter, M. A Study on Electrolyte Interactions with Graphite Anodes Exhibiting Structures with Various Amounts of Rhombohedral Phase. *J. Power Sources* **2003**, *119*, 528−537.
(8) Kasavajjula, U.; Wang, C. S.; Appleby, A. J. Nano- and Bulk-Silicon-Based Insertion Anodes for Lithium-Ion Secondary Cells. *J. Power Sources* **2007**, *163* (2), 1003−1039.
(9) Obrovac, M. N.; Christensen, L. Structural Changes in Silicon Anodes During Lithium Insertion/Extraction. *Electrochem. Solid-State Lett.* **2004**, *7* (5), A93−A96.
(10) Besenhard, J. O.; Yang, J.; Winter, M. Will Advanced Lithium-Alloy Anodes Have a Chance in Lithium-Ion Batteries? *J. Power Sources* **1997**, *68* (1), 87−90.
(11) Winter, M.; Besenhard, J. O.; Albering, J. H.; Yang, J.; Wachtler, M. Lithium Storage Alloys as Anode Materials in Lithium Ion Batteries. *Prog. Batteries Battery Mater.* **1998**, *17*, 208−213.
(12) Liu, W. R.; Wang, J. H.; Wu, H. C.; Shieh, D. T.; Yang, M. H.; Wu, N. L. Electrochemical Characterizations on Si and C-Coated Si Particle Electrodes for Lithium-Ion Batteries. *J. Electrochem. Soc.* **2005**, *152* (9), A1719−A1725.
(13) Courtel, F. M.; Duguay, D.; Abu-Lebdeh, Y.; Davidson, I. J. Investigation of Crsi2 and Mosi2 as Anode Materials for Lithium-Ion Batteries. *J. Power Sources* **2012**, *202*, 269−275.
(14) Hwang, S. M.; Lee, H. Y.; Jang, S. W.; Lee, S. M.; Lee, S. J.; Baik, H. K.; Lee, J. Y. Lithium Insertion in Siag Powders Produced by Mechanical Alloying. *Electrochem. Solid-State Lett.* **2001**, *4* (7), A97−A100.
(15) Jia, H. P.; Stock, C.; Kloepsch, R.; He, X.; Badillo, J. P.; Fromm, O.; Vortmann, B.; Winter, M.; Placke, T. Facile Synthesis and Lithium Storage Properties of a Porous Nisi2/Si/Carbon Composite Anode Material for Lithium-Ion Batteries. *ACS Appl. Mater. Interfaces* **2015**, *7* (3), 1508−1515.
(16) Liu, W. R.; Wu, N. L.; Shieh, D. T.; Wu, H. C.; Yang, M. H.; Korepp, C.; Besenhard, J. O.; Winter, M. Synthesis and Characterization of Nanoporous Nisi-Si Composite Anode for Lithium-Ion Batteries. *J. Electrochem. Soc.* **2007**, *154* (2), A97−A102.
(17) Chen, Y.; Qian, J. F.; Cao, Y. L.; Yang, H. X.; Ai, X. P. Green Synthesis and Stable Li-Storage Performance of Fesi2/Si@C Nanocomposite for Lithium-Ion Batteries. *ACS Appl. Mater. Interfaces* **2012**, *4* (7), 3753−3758.
(18) Wang, G. X.; Sun, L.; Bradhurst, D. H.; Zhong, S.; Dou, S. X.; Liu, H. K. Nanocrystalline Nisi Alloy as an Anode Material for Lithium-Ion Batteries. *J. Alloys Compd.* **2000**, *306* (1−2), 249−252.
(19) Lee, K. M.; Lee, Y. S.; Kim, Y. W.; Sun, Y. K.; Lee, S. M. Electrochemical Characterization of Ti-Si and Ti-Si-Al Alloy Anodes for Li-Ion Batteries Produced by Mechanical Ball Milling. *J. Alloys Compd.* **2009**, *472* (1−2), 461−465.
(20) Nayeb-Hashemi, A. A.; Clark, J. B. The Mg-Si (Magnesium-Silicon) System. *Bull. Alloy Phase Diagrams* **1984**, *5* (6), 584−592.
(21) Xiao, C. M.; Du, N.; Zhang, H.; Yang, D. R. Improved Cyclic Stability of Mg2si by Direct Carbon Coating as Anode Materials for Lithium-Ion Batteries. *J. Alloys Compd.* **2014**, *587*, 807−811.
(22) Moriga, T.; Watanabe, K.; Tsuji, D.; Massaki, S.; Nakabayashi, I. Reaction Mechanism of Metal Silicide Mg2si for Li Insertion. *J. Solid State Chem.* **2000**, *153* (2), 386−390.
(23) Song, S. W.; Striebel, K. A.; Song, X. Y.; Cairns, E. J. Amorphous and Nanocrystalline Mg2si Thin-Film Electrodes. *J. Power Sources* **2003**, *119*, 110−112.
(24) Ma, R. J.; Liu, Y. F.; Yang, Y. X.; Gao, M. X.; Pan, H. G. Mg_2Si Anode for Li-Ion Batteries: Linking Structural Change to Fast Capacity Fading. *Appl. Phys. Lett.* **2014**, *105* (21), 213901.
(25) Roberts, G. A.; Cairns, E. J.; Reimer, J. A. Magnesium Silicide as a Negative Electrode Material for Lithium-Ion Batteries. *J. Power Sources* **2002**, *110* (2), 424−429.
(26) Kim, H.; Choi, J.; Sohn, H. J.; Kang, T. The Insertion Mechanism of Lithium into Mg2si Anode Material for Li-Ion Batteries. *J. Electrochem. Soc.* **1999**, *146* (12), 4401−4405.
(27) Shi, Z.; Liu, M. L.; Naik, D.; Gole, J. L. Electrochemical Properties of Li-Mg Alloy Electrodes for Lithium Batteries. *J. Power Sources* **2001**, *92* (1−2), 70−80.
(28) Zhang, W. J. Lithium Insertion/Extraction Mechanism in Alloy Anodes for Lithium-Ion Batteries. *J. Power Sources* **2011**, *196* (3), 877−885.
(29) Voutsas, A. T.; Hatalis, M. K.; Boyce, J.; Chiang, A. Raman Spectroscopy of Amorphous and Microcrystalline Silicon Films Deposited by Low-Pressure Chemical Vapor Deposition. *J. Appl. Phys.* **1995**, *78* (12), 6999−7006.
(30) Onari, S.; Cardona, M. Resonant Raman-Scattering in Ii-Iv Semiconductors Mg2si, Mg2ge, and Mg2sn. *Phys. Rev. [Sect] B* **1976**, *14* (8), 3520−3531.
(31) Baleva, M.; Zlateva, G.; Atanassov, A.; Abrashev, M.; Goranova, E. Resonant Raman Scattering in Ion-Beam-Synthesized Mg2Si in a Silicon Matrix. *Phys. Rev. B: Condens. Matter Mater. Phys.* **2005**, *72* (11), 115330.
(32) Whitten, W. B.; Chung, P. L.; Danielson, G. C. Elastic Constants and Lattice Vibration Frequencies of Mg2si. *J. Phys. Chem. Solids* **1965**, *26* (1), 49−56.
(33) Song, S. W.; Striebel, K. A.; Reade, R. P.; Roberts, G. A.; Cairns, E. J. Electrochemical Studies of Nanoncrystalline Mg2si Thin Film Electrodes Prepared by Pulsed Laser Deposition. *J. Electrochem. Soc.* **2003**, *150* (1), A121−A127.
(34) Buchenauer, C. J.; Cardona, M. Raman Scattering in Mg2Si, Mg2Ge, and Mg2Sn. *Phys. Rev. [Sect] B* **1971**, *3* (8), 2504−2507.
(35) Onari, S.; Cardona, M. Resonant Raman-Scattering in II-IV Semiconductors Mg_2Si, Mg_2Ge, and Mg_2Sn. *Phys. Rev. B* **1976**, *14* (8), 3520−3531.
(36) Takamura, T.; Ohara, S.; Uehara, M.; Suzuki, J.; Sekine, K. A Vacuum Deposited Si Film Having a Li Extraction Capacity over 2000 Mah/G with a Long Cycle Life. *J. Power Sources* **2004**, *129* (1), 96−100.
(37) Lee, K. L.; Jung, J. Y.; Lee, S. W.; Moon, H. S.; Park, J. W. Electrochemical Characteristics of a-Si Thin Film Anode for Li-Ion Rechargeable Batteries. *J. Power Sources* **2004**, *129* (2), 270−274.
(38) Moon, T.; Kim, C.; Park, B. Electrochemical Performance of Amorphous-Silicon Thin Films for Lithium Rechargeable Batteries. *J. Power Sources* **2006**, *155* (2), 391−394.
(39) Schranzhofer, H.; Bugajski, J.; Santner, H. J.; Korepp, C.; Möller, K. C.; Besenhard, J. O.; Winter, M.; Sitte, W. Electrochemical Impedance Spectroscopy Study of the Sei Formation on Graphite and Metal Electrodes. *J. Power Sources* **2006**, *153* (2), 391−395.
(40) Krueger, S.; Kloepsch, R.; Li, J.; Nowak, S.; Passerini, S.; Winter, M. How Do Reactions at the Anode/Electrolyte Interface Determine the Cathode Performance in Lithium-Ion Batteries? *J. Electrochem. Soc.* **2013**, *160* (4), A542−A548.
(41) Smith, A. J.; Burns, J. C.; Dahn, J. R. A High Precision Study of the Coulombic Efficiency of Li-Ion Batteries. *Electrochem. Solid-State Lett.* **2010**, *13* (12), A177−A179.
(42) Besenhard, J. O.; Wagner, M. W.; Winter, M.; Jannakoudakis, A. D.; Jannakoudakis, P. D.; Theodoridou, E. Inorganic Film-Forming Electrolyte Additives Improving the Cycling Behavior of Metallic Lithium Electrodes and the Self-Discharge of Carbon Lithium Electrodes. *J. Power Sources* **1993**, *44* (1−3), 413−420.
(43) Xu, K. Nonaqueous Liquid Electrolytes for Lithium-Based Rechargeable Batteries. *Chem. Rev.* **2004**, *104* (10), 4303−4417.
(44) Obrovac, M. N.; Krause, L. J. Reversible Cycling of Crystalline Silicon Powder. *J. Electrochem. Soc.* **2007**, *154* (2), A103−A108.

DOI: 10.1021/acsami.5b05382
ACS Appl. Mater. Interfaces 2015, 7, 20124−20133

(45) Park, C. M.; Kim, Y. U.; Kim, H.; Sohn, H. J. Enhancement of the Rate Capability and Cyclability of an Mg-C Composite Electrode for Li Secondary Batteries. *J. Power Sources* **2006**, *158* (2), 1451−1455.
(46) Ender, M.; Weber, A.; Ivers-Tiffee, E. Analysis of Three-Electrode Setups for Ac-Impedance Measurements on Lithium-Ion Cells by Fem Simulations. *J. Electrochem. Soc.* **2012**, *159* (2), A128−A136.
(47) Etacheri, V.; Haik, O.; Goffer, Y.; Roberts, G. A.; Stefan, I. C.; Fasching, R.; Aurbach, D. Effect of Fluoroethylene Carbonate (Fec) on the Performance and Surface Chemistry of Si-Nanowire Li-Ion Battery Anodes. *Langmuir* **2012**, *28* (1), 965−976.
(48) Aurbach, D.; Markovsky, B.; Weissman, I.; Levi, E.; Ein-Eli, Y. On the Correlation between Surface Chemistry and Performance of Graphite Negative Electrodes for Li Ion Batteries. *Electrochim. Acta* **1999**, *45* (1−2), 67−86.
(49) Vetter, J.; Novak, P.; Wagner, M. R.; Veit, C.; Möller, K. C.; Besenhard, J. O.; Winter, M.; Wohlfahrt-Mehrens, M.; Vogler, C.; Hammouche, A. Ageing Mechanisms in Lithium-Ion Batteries. *J. Power Sources* **2005**, *147* (1−2), 269−281.
(50) Andre, D.; Meiler, M.; Steiner, K.; Wimmer, C.; Soczka-Guth, T.; Sauer, D. U. Characterization of High-Power Lithium-Ion Batteries by Electrochemical Impedance Spectroscopy. I. Experimental Investigation. *J. Power Sources* **2011**, *196* (12), 5334−5341.
(51) Ruffo, R.; Hong, S. S.; Chan, C. K.; Huggins, R. A.; Cui, Y. Impedance Analysis of Silicon Nanowire Lithium Ion Battery Anodes. *J. Phys. Chem. C* **2009**, *113* (26), 11390−11398.

DOI: 10.1021/acsami.5b05382
ACS Appl. Mater. Interfaces 2015, 7, 20124−20133